

RadJEPa: Radiology Encoder for Chest X-Rays via Joint Embedding Predictive Architecture

Anas Khan¹ Mariam Husain² Kshitij Jadhav³

¹Department of Computer Science and Engineering, Indian Institute of Technology Bombay, India

²Department of Biomedical Engineering, Johns Hopkins University, USA

³Koita Centre for Digital Health, Indian Institute of Technology Bombay, India

anaskhan@cse.iitb.ac.in mhusai10@jh.edu kshitij.jadhav@iitb.ac.in

Abstract

Recent advances in medical vision–language models guide the learning of visual representations; however, this form of supervision is constrained by the availability of paired image–text data, raising the question of whether robust radiology encoders can be learned without relying on language supervision. In this work, we introduce RadJEPa, a self-supervised framework built on a Joint Embedding Predictive Architecture that learns without language supervision. Pre-trained solely on unlabeled chest X-ray images, the model learns to predict latent representations of masked image regions. This predictive objective differs fundamentally from both image–text pre-training and DINO-style self-distillation: rather than aligning global representations across views or modalities, RadJEPa explicitly models latent-space prediction. We evaluate the learned encoder on disease classification, semantic segmentation, and report generation task. Across benchmarks, RadJEPa achieves performance exceeding state-of-the-art approaches including RAD-DINO. Code and pre-trained model weights are made publicly available on GitHub¹ and Hugging Face².

1 Introduction

Vision–language modeling has largely been driven by the use of textual supervision (Desai and Johnson, 2021; Radford et al., 2021). In biomedical imaging (Boecking et al., 2022; Zhou et al., 2023), these representations are often reused as fixed visual tokens for downstream reasoning, such as report generation, Image Classification, Segmentation. This paradigm implicitly assumes that textual descriptions provide a sufficiently complete and unbiased account of visual content (Dehghani et al., 2023). Radiology reports are written to support clinical decision making and therefore emphasize

selective findings, frequently omitting subtle variations, or absent observations. As a result, visual encoders trained to align images with text may inherit bias (Jones et al., 2024) and fail to preserve the full semantic structure present in medical images.

Beyond language supervision, recent self-supervised approaches such as DINO-style self-distillation have emerged as powerful alternatives for representation learning without labels (Oquab et al., 2023). These methods learn invariances by aligning global representations across multiple augmented views of the same image using a teacher–student formulation. In the context of chest X-rays (Perez-Garcia et al., 2025), where fine-grained anatomical differences and subtle pathological cues are often diagnostically relevant, enforcing global agreement across views can lead to representations that prioritize appearance-level consistency over semantic completeness. Moreover, self-distillation methods (Dong et al., 2023) emphasize consistency across pixel-space (view-centric) augmentations, rather than predicting semantic representations in latent space.

Why Predictive Latent Modeling We argue that chest X-rays are fundamentally *semantic* rather than view-centric (Çalli et al., 2021): clinical interpretation depends on global anatomical context, spatial relationships, and subtle deviations from normal structure. Consequently, learning representations directly in pixel space or enforcing view-level invariance may not be the most appropriate. Instead, we adopt a *predictive latent modeling* perspective (Assran et al., 2023a). Formally, given an image x , we partition it into visible regions x_v and masked regions x_m . An encoder f_θ maps these regions into latent representations $z_v = f_\theta(x_v)$ and $z_m = f_\theta(x_m)$. A predictor g_ϕ is then trained to predict the latent representation of the masked regions from the latent representation of visible context by

¹<https://github.com/aidelab-iitbombay/RadJEPa>

²<https://huggingface.co/AIDElab-IITBombay/RadJEPa>

minimizing:

$$\mathcal{L} = \|g_\phi(z_v) - \text{stopgrad}(z_m)\|^2.$$

Our main contributions are as follows:

- We show that language supervision and DINO-style self-supervised distillation have limitations in radiological representation learning. We introduce **RadJEPA**, a predictive self-supervised architecture that achieves performance comparable to or exceeding SoTA models trained on over 839k chest X-ray images.
- We provide empirical evaluations of RadJEPA across three downstream tasks, classification, segmentation, and report generation. We benchmark against a diverse set of baselines, including larger-capacity architectures.

2 Related Work

Contrastive learning has been a dominant paradigm for visual representation learning, relying on instance-level discrimination through positive and negative pairs (Oord et al., 2018; Chen et al., 2020; He et al., 2020). This formulation has been extended to multimodal settings, most notably in CLIP-style image-text models that align visual and textual embeddings in a shared latent space (Radford et al., 2021). While effective, contrastive objectives are known to induce representational invariances that may suppress fine-grained visual details and intra-class variability, particularly when supervision is incomplete or biased (Zhai et al., 2022; Liang et al., 2022). Such limitations are especially relevant in medical imaging, anatomical differences are critical for downstream analysis.

Masked image modeling (MIM) and self-distillation approaches aim to reduce reliance on contrastive negatives and paired supervision. MIM-based methods learn contextualized representations by reconstructing masked regions or tokens (Bao et al., 2022; He et al., 2022), demonstrating strong scalability and transferability. Complementary to this, self-distillation and clustering-based frameworks such as DINO enforce consistency across multiple augmented views without explicit negatives (Caron et al., 2021). Recent large-scale variants (e.g., DINoV2) further show strong domain-transfer capabilities and applicability to dense prediction tasks (Oquab et al., 2023). However, these approaches typically depend on pixel-level reconstruction or handcrafted augmentation strategies.

Predictive learning frameworks have been proposed to address these limitations by learning representations through latent-space prediction rather than reconstruction or contrastive matching (Le-Cun, 2022). Joint-Embedding Predictive Architectures (JEPA) formalize this idea by predicting abstract representations of masked or future regions, emphasizing semantic abstraction and representational stability (Assran et al., 2023b). Recent adaptations of this paradigm to neuroimaging, such as BrainJEPA, have demonstrated promising results in learning transferable and cognitively meaningful representations from brain signals without task-specific supervision (Dong et al., 2024). Despite these advances, predictive architectures remain relatively underexplored in medical imaging (Zhou et al., 2019; Tang et al., 2022).

3 Methodology

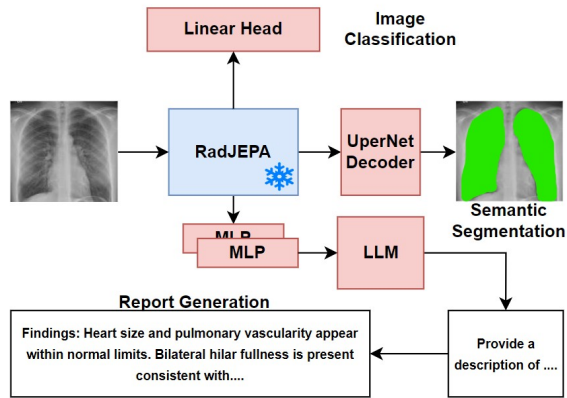


Figure 1: RadJEPA frozen encoder with trainable task-specific heads.

3.1 RadJEPA Pretraining

Let $x \in \mathbb{R}^{H \times W}$ denote an input chest X-ray. Two non-overlapping regions are sampled: a context region c and a target region t . A visual encoder f maps image regions to latent representations. A predictor network g projects the context embedding to the target embedding space:

$$z_c = f(c), \quad z_t = f(t), \quad \hat{z}_t = g(z_c)$$

RadJEPA is trained using a latent prediction objective. The objective operates entirely in representation space, without pixel reconstruction, contrastive negatives, or data augmentations.

$$\mathcal{L}_{\text{JEPA}} = \mathbb{E}_{(c,t)} \left[\| \text{stopgrad}(z_t) - \hat{z}_t \|_2^2 \right]$$

The parameters of the target encoder f' are not optimized by gradient descent, but updated as an exponential moving average (EMA) of the online encoder f . $\tau \in [0, 1]$ is the momentum coefficient.

$$\theta' \leftarrow \tau \theta' + (1 - \tau) \theta$$

Downstream Usage: After pretraining, the visual encoder f is frozen and reused across all downstream tasks. Task-specific heads or adapters are trained independently.

3.2 Disease Classification

Given an image x , frozen features are extracted and a linear classifier W predicts class probabilities. Only the linear head is optimized.

$$h = f(x), \quad p = \text{softmax}(Wh),$$

$$\mathcal{L}_{\text{cls}} = - \sum_{k=1}^K y_k \log p_k$$

3.3 Semantic Segmentation

Multi-scale feature maps are extracted from the frozen encoder. A UperNet decoder \mathcal{D} aggregates hierarchical features to produce pixel-wise logits. Only decoder parameters are trained.

$$\{h_l\}_{l=1}^L = f^{(l)}(x), \quad S = \mathcal{D}(\{h_l\})$$

$$\mathcal{L}_{\text{seg}} = - \sum_{i,j} \sum_{c=1}^C y_{ij}^c \log \text{softmax}(S_{ij}^c)$$

3.4 Report Generation

We follow a LLaVA-style multimodal formulation, extracting frozen visual embeddings $v = f(x)$ from the input image. A lightweight two-layer projection adapter A maps visual features into the language embedding space.

$$\tilde{v} = A(v) = v + \lambda W_2 \sigma(W_1 v),$$

The projected embeddings are concatenated with an instruction prompt and provided as input to a language model \mathcal{M} .

$$p(y_t \mid y_{<t}, x) = \mathcal{M}(y_t \mid y_{<t}, \tilde{v})$$

The report generation objective is the autoregressive negative log-likelihood.

$$\mathcal{L}_{\text{txt}} = - \sum_{t=1}^T \log p(y_t \mid y_{<t}, x)$$

During training, the visual encoder f is frozen, while both the adapter parameters and the language model parameters are optimized jointly.

4 RadJEPA Pretraining Setup

RadJEPA pretraining follows the Meta I-JEPA protocol (Assran et al., 2023a), as described in Section 3.1 and Figure 1. We adopt a data configuration closely aligned with RAD-DINO (Pérez-García et al., 2024), leveraging large-scale chest X-ray datasets summarized in Table 1. In the publicly available data, frontal-view images substantially outnumber lateral-view images, resulting in an approximate 6:1 frontal-to-lateral ratio. Unlike RAD-DINO, which additionally incorporates approximately 90k images from proprietary sources, we rely solely on open-source datasets. To reduce the resulting viewpoint imbalance, we augment the lateral-view subset by adding approximately 90k lateral chest X-rays from MIMIC-CXR, yielding a final frontal-to-lateral ratio of approximately 3:1. Overall, RadJEPA is pretrained on 839,364 chest X-ray images, as detailed in Table 1.

5 Comparison with Baselines

A set of baseline approaches is considered for experimental analysis (Table 2), with RAD-DINO serving as a key image-only baseline that empirically shows large-scale image–text supervision is not always optimal for learning robust chest X-ray representations. Comparison with other image-only self-supervised methods is outside the scope of this study, as it has been extensively explored in prior work (Oquab et al., 2023; Huang et al., 2023; Caron et al., 2021). Building on this observation, RadJEPA explores predictive self-supervised learning in latent space to better capture radiological semantics. Unlike view-augmentation-based methods that focus on pixel-level invariances, RadJEPA predicts masked regions in representation space, encouraging modeling of high-level semantic structure while suppressing low-level noise.

As summarized in Table 2, RadJEPA is using a ViT-B/14 backbone. This design choice is intentional: despite its relatively smaller capacity, the ViT-B/14 RadJEPA encoder consistently outperforms significantly larger models. These results indicate that performance gains are not solely driven by model scale, but by the quality of the learned representations. An advantage of JEPA-style architectures is their improved sample efficiency, often achieving better performance with fewer training images compared to alternative architectures, important for chest X-rays, where available datasets are much smaller than natural image collections.

Dataset	View	Patient cohort	#Subjects	#Images	Frontal	Lateral
BRAX (Reis et al., 2022)	frontal, lateral	institutional PACS	19,351	41,620	24,959	16,661
CheXpert (Irvin et al., 2019)	frontal, lateral	inpatient, outpatient	65,240	224,316	191,229	33,087
MIMIC-CXR (Johnson et al., 2019)	frontal, lateral	ICU	188,546	300,491	210,491	90,000
ChestX-ray14 (Wang et al., 2017)	frontal	not specified	32,717	112,120	112,120	0
PadChest (Bustos et al., 2020)	frontal, lateral	all available	67,000	160,817	96,287	64,530
Total			372,854	839,364	635,086	204,278

Table 1: Chest X-ray datasets used for RadJEPA pretraining. For MIMIC-CXR, only a subset of subjects is included to avoid overlap with evaluation sets.

Model type	Model	Arch.	# Params.	Training dataset	# Images	# Text	Resolution
Image & Text	CLIP@224 (Radford et al., 2021)	ViT-L/14	304 M	WebImageText	400 M	400 M	224 ²
Image & Text	CLIP@336 (Radford et al., 2021)	ViT-L/14	304 M	WebImageText	400 M	400 M	336 ²
Image & Text	BioViL (Bannur et al., 2023)	ResNet50	27 M	MIMIC-CXR	197 k	174 k	512 ²
Image & Text	BioMedCLIP (Zhang et al., 2023)	ViT-B/16	86 M	PMC-15M	15 M	15 M	224 ²
Image & Text	CheXzero (Tiu et al., 2022)	ViT-B/32	151 M	MIMIC-CXR	377 k	227 k	224 ²
Image & Text	MRM (Zhou et al., 2023)	ViT-B/16	86 M	MIMIC-CXR	377 k	227 k	448 ²
Image Only	DINO-v2 (Oquab et al., 2023)	ViT-G/14	1.1 B	LVD	142 M	–	518 ²
Image Only	RAD-DINO _{control}	ViT-B/14	87 M	MIMIC-CXR	197 k	–	518 ²
Image Only	RAD-DINO (Pérez-García et al., 2024)	ViT-B/14	87 M	Multi-CXR	838 k	–	518 ²
Image (Predictive)	I-JEPA (Assran et al., 2023a)	ViT-H/14	0.6 B	IN1K	1.28 M	–	448 ²
Image (Predictive)	RadJEPA _{control}	ViT-B/14	86 M	MIMIC-CXR	197 k	–	224 ²
Image (Predictive)	RadJEPA	ViT-B/14	86 M	Multi-CXR	839 k	–	224 ²

Table 2: Overview of image backbones and their training dataset characteristics employed in experimental analysis.

6 Evaluation on Downstream Tasks.

6.1 Image Classification

6.1.1 Datasets

We evaluate all models on two external chest X-ray (CXR) benchmarks: VinDr-CXR and RSNA-Pneumonia. Implementation details are provided in Section 6.1.2.

VinDr-CXR (Nguyen et al., 2022) is a multi-label CXR dataset with expert annotations covering a diverse set of thoracic findings, ranging from large anatomical abnormalities (e.g., cardiomegaly, aortic enlargement) to subtle texture-based pathologies (e.g., pulmonary fibrosis, tuberculosis). We use a subset of six findings and follow a 15,000/3,000 train/test split by subject, resulting in 18,000 images from 18,000 unique patients.

RSNA-Pneumonia (Anouk Stein et al., 2018) focuses on pneumonia detection from frontal chest X-rays and primarily captures acute lung opacities. The dataset contains 26,684 images from the same number of subjects, and we follow a 60/20/20 train/validation/test split by subject.

6.1.2 Implementation details

All datasets are split by subject identifier to prevent patient-level leakage. We evaluate RadJEPA

on VinDr-CXR using 15,000 training images and 3,000 test images, and on the RSNA Pneumonia Detection dataset as a binary classification task with a 60/20/20 train/validation/test split by subject. Images are converted to single-channel grayscale and preprocessed using center cropping and resizing, with training-time augmentations including random horizontal flipping, affine transformations, random cropping, color jittering, and additive Gaussian noise. Image classification is performed via linear probing, where a linear classifier with sigmoid activation is trained on the frozen 768-dimensional global image embedding using binary cross-entropy loss. Optimization uses AdamW with a learning rate of 5×10^{-5} and a cosine learning rate schedule. All experiments are conducted on **3 NVIDIA A6000 GPUs** with a batch size of 32 per GPU (total batch size 96) for 100 epochs, and results are reported as the mean and standard deviation of the Area Under the Precision–Recall Curve (AUPRC) over 5-fold cross-validation.

6.1.3 Results analysis

Table 3 summarizes performance on VinDr-CXR and RSNA-Pneumonia. Across both datasets, *RadJEPA consistently outperforms all competing image-only and vision-language pretraining baselines*. On VinDr-CXR, RadJEPA achieves the high-

Model	VinDr-CXR (AP)							RSNA	
	LO	CM	PL-T	AE	PF	PE	Agg.	AP	AUC
CLIP@224	9.7	42.6	18.8	30.0	24.1	21.8	23.8	60.1	83.7
CLIP@336	9.1	46.1	18.5	29.0	22.8	18.6	23.4	60.0	84.2
BioViL-T	12.7	51.4	24.6	22.3	30.5	52.2	32.4	66.8	86.9
BiomedCLIP	10.0	58.5	24.4	36.2	32.0	54.1	35.9	68.4	87.5
CheXzero	11.1	74.4	25.1	42.9	33.1	60.2	40.0	68.9	87.9
MRM	12.2	79.7	35.8	47.7	47.1	77.2	51.3	71.4	89.0
RAD-DINO	14.9	69.9	36.6	44.6	59.4	77.8	52.8	71.0	88.4
RAD-DINO*	14.2	68.4	35.8	48.5	57.2	74.9	49.8	69.1	86.8
I-JEPA	15.6	70.3	36.8	47.9	59.0	70.5	50.0	70.2	87.4
RadJEPA	19.2	72.6	42.2	58.6	63.9	74.4	55.2	72.7	89.2

Table 3: Image classification performance with linear probing on VinDr-CXR and RSNA-Pneumonia. AP denotes area under the precision-recall curve (AUPRC) and AUC denotes area under the ROC curve (AUROC). Agg. denotes mean AUPRC over the six VinDr-CXR classes: LO (Lung Opacity), CM (Cardiomegaly), PL-T (Pleural Thickening), AE (Aortic Enlargement), PF (Pulmonary Fibrosis), and PE (Pleural Effusion). (*) denotes reproduced result. VinDr-CXR uses 15,000/3,000 train/test splits; RSNA-Pneumonia results are reported on the test set (5,337 images). Results are averaged over five random seeds.

est mean AUPRC (Agg.) of **55.2**, surpassing RAD-DINO (52.8), I-JEPA (50.0), and the strongest vision-language baseline MRM (51.3). On RSNA-Pneumonia, RadJEPA attains the best AUPRC (**72.7**) and AUROC (**89.2**). RadJEPA shows particularly strong improvements on subtle and heterogeneous findings such as pulmonary lesions (PL-T), aortic enlargement (AE), and pulmonary fibrosis (PF), achieving the highest AUPRC across all methods; for instance, it improves PF detection by **+4.5 AUPRC** over RAD-DINO and **+4.9 AUPRC** over I-JEPA. Compared to the original I-JEPA, RadJEPA yields consistent gains across all VinDr-CXR classes. Importantly, as shown in Table 2, RadJEPA employs a ViT-B/14 backbone with only **86M parameters**, which is substantially smaller than DINO-v2 (1.1B parameters) and I-JEPA (0.6B parameters), yet achieves superior downstream performance.

6.2 Semantic Segmentation

6.2.1 Datasets

All splits are performed by subject identifier to avoid data leakage. Implementation details are provided in Section 6.2.2.

Lung and Lung Zone Segmentation Lung segmentation masks are obtained from a publicly available dataset derived from MIMIC-CXR (Johnson et al., 2019). To construct lung zone annotations, bounding boxes corresponding to six lung regions

(left upper, left middle, left lower, right upper, right middle, right lower) are sourced from the Chest ImaGenome dataset (Wu et al., 2021) and applied to the corresponding MIMIC-CXR images. This results in 1,138 images from 1,138 subjects with annotations for both left/right lungs and lung zones.

Rib Segmentation For rib segmentation, we use the VinDR-RibCXR dataset (Nguyen et al., 2021), which provides expert annotations for 20 individual ribs (L1-L10, R1-R10). The dataset contains images from 245 subjects and is used with the official train/test splits.

6.2.2 Implementation details

We evaluate RadJEPA for semantic segmentation using frozen backbone encoders with task-specific decoder heads. Experiments are conducted on a single compute node with **4 NVIDIA A6000 GPUs**, using a batch size of 20 per GPU (total batch size 80). We optimize the segmentation models using the Adam optimizer with a base learning rate of 5×10^{-4} and a cosine learning rate scheduler. Images are preprocessed using center cropping and resizing, with training-time augmentations including random horizontal flipping (except for left-right lung and lung zone tasks), random affine and elastic transformations, brightness and contrast jittering, and random gamma adjustments. We normalise image intensities using statistics computed from all images in MIMIC-CXR (Johnson et al., 2019).

Encoder	Decoder	# Features	# Params	Lungs	Lung zones	Ribs
NN-UNet (Isensee et al., 2018)	Unet	–	17.9 M	98.0	92.6	86.2
EfficientNet-B6 (Tan and Le, 2019)	Unet	–	45.9 M	98.3	92.7	88.9
BioViL-T (Bannur et al., 2023)	Linear	2048	2049	83.2	69.4	59.1
BiomedCLIP (Zhang et al., 2023)	Linear	768	769	90.4	76.2	67.4
CheXzero (Tiu et al., 2022)	Linear	768	769	84.0	68.3	62.0
RAD-DINO (no MIM)	Linear	768	769	91.3	78.8	67.3
RAD-DINO	Linear	768	769	95.9	85.7	73.4
RAD-DINO	ViTDet (Li et al., 2022)	4×768	24.8 M	97.8	90.7	83.6
RAD-DINO	UPerNet (Xiao et al., 2018)	4×768	39.3 M	98.0	91.2	85.3
RAD-DINO*	UPerNet (Xiao et al., 2018)	4×768	39.3 M	98.1	91.5	84.8
I-JEPA	UPerNet (Xiao et al., 2018)	4×768	39.3 M	97.9	92.0	85.2
RadJEPA	UPerNet (Xiao et al., 2018)	4×768	39.3 M	98.3	93.7	89.6

Table 4: Semantic segmentation results obtained with linear, ViTDet, and UPerNet decoders on frozen backbone encoders. Dice scores are reported as mean. Lungs denote left and right lung segmentation, Lung zones correspond to six anatomical lung regions, and Ribs refer to rib segmentation. End-to-end U-Net models indicate upper-bound performance. (*) denotes reproduced result.

Models are trained for 100 epochs using a 70/15/15 train/validation/test split by subject, and evaluation is performed on the test set using the checkpoint with the lowest validation loss (for rib segmentation, we use the official split of 196 training and 49 test images).

6.2.3 Results analysis

Table 4 reports semantic segmentation performance. Across all segmentation tasks, *RadJEPA* consistently outperforms competing image-only and vision-language pretrained backbones under identical decoder configurations. With a UPerNet decoder, RadJEPA achieves the highest Dice scores on lung (**98.3**), lung zone (**93.7**), and rib (**89.6**) segmentation, surpassing RAD-DINO and I-JEPA across all three tasks. Notably, RadJEPA shows the largest gains on structurally complex targets such as lung zones and ribs, improving rib segmentation by **+4.8 Dice** over RAD-DINO and **+4.4 Dice** over I-JEPA, indicating stronger spatial and anatomical representation learning. Importantly, all predictive and contrastive baselines share the same decoder architecture and parameter count, highlighting that RadJEPA’s improvements stem from more informative pretrained representations rather than decoder.

6.3 Report Generation

6.3.1 Datasets

We evaluate report generation on two datasets, MIMIC-CXR and IU-Xray. Implementation details are provided in Section 6.3.2.

MIMIC-CXR For report generation, we use the official MIMIC-CXR dataset and follow the same train/validation/test splits used for RAD-DINO (Pérez-García et al., 2024). We retain only frontal chest X-rays with an associated *Findings* section, resulting in 146,909 image-text pairs for training, 7,250 for validation, and 2,461 for testing. These splits are used exclusively to fine-tune language decoder, while the encoder remains frozen.

IU-Xray To evaluate generalization beyond the training distribution, we additionally report results on the IU-Xray dataset, which is not used during training of either the image encoder or the language decoder. The IU-Xray test set contains 3,306 studies and provides an out-of-distribution benchmark for assessing report generation performance on a distinct clinical dataset.

6.3.2 Implementation details

We follow a LLaVA-style architecture (Liu et al., 2023b,a). Patch embeddings from the frozen image encoder are projected and concatenated with an instruction to generate an output report: “⟨image_tokens⟩ Provide a description of the findings in the radiology image.” Following LLaVA-1.5 (Liu et al., 2023a), we use a two-layer fully connected (MLP) projector and Vicuna-7B (v1.5) (Chiang et al., 2023) as the language model. The projection network is initialised with random weights, while the image encoder is frozen. Input information to the LLM is kept minimal to focus evaluation on the quality of the image representations. Training is performed on four NVIDIA A100 GPU

Dataset	Image encoder	Input res.	# Tokens	ROUGE-L	BLEU-4	R _{GER}	Macro-F1-14
MIMIC	CLIP@224(Radford et al., 2021)	224×224	256	23.0	8.3	20.3	24.7
	CLIP@336(Radford et al., 2021)	316×316	576	23.3	8.4	20.4	25.3
	DINO-v2 (Oquab et al., 2023)	518×518	1369	22.7	7.6	18.5	18.6
	BiomedCLIP (Zhang et al., 2023)	224×224	256	23.1	7.9	20.4	24.9
	CheXzero (Tiu et al., 2022)	224×224	49	23.2	8.0	20.6	26.2
	BioViL(Bannur et al., 2023)	512×512	196	23.5	7.3	22.4	28.4
	RAD-DINO _{control}	518×518	1369	24.2	9.0	22.4	31.5
	RAD-DINO	518×518	1369	24.6	9.3	22.8	31.9
	RAD-DINO*	518×518	1369	25.1	9.4	23.2	32.0
	I-JEPA	224×224	1369	25.6	9.5	23.4	32.1
IU	RadJEPA _{control}	224×224	1369	25.5	9.7	23.3	31.9
	RadJEPA	224×224	1369	26.1	10.1	23.8	32.6
	CLIP@224(Radford et al., 2021)	224×224	256	25.4	9.2	25.8	18.1
	CLIP@336(Radford et al., 2021)	316×316	576	25.3	8.0	25.3	18.5
	DINO-v2 (Oquab et al., 2023)	518×518	1369	25.4	8.0	23.6	12.3
IU	BiomedCLIP (Zhang et al., 2023)	224×224	256	20.2	6.3	20.0	7.1
	CheXzero (Tiu et al., 2022)	224×224	49	25.6	8.5	25.7	18.1
	BioViL(Bannur et al., 2023)	512×512	196	26.3	8.2	25.3	20.2
	RAD-DINO _{control}	518×518	1369	25.5	9.2	26.2	23.8
	RAD-DINO	518×518	1369	25.8	9.0	26.2	25.5
IU	RAD-DINO*	518×518	1369	26.3	9.4	26.6	26.4
	I-JEPA	224×224	1369	26.7	9.4	26.8	26.3
	RadJEPA _{control}	224×224	1369	27.1	9.6	27.0	26.8
	RadJEPA	224×224	1369	28.4	9.9	27.5	27.6

Table 5: Downstream radiology report generation results on MIMIC-CXR and IU-Xray. All models use a two-layer MLP projector and Vicuna-7B (v1.5) (Zheng et al., 2023) to generate the *Findings* section. We report median and 95% confidence intervals from 500 bootstrap samples. (*) denotes reproduced result.

compute nodes with 80GB RAM. We use the same hyperparameters as LLaVA-1.5, including a cosine learning rate scheduler with a base learning rate of 2×10^{-5} , a batch size of 128 (32 per GPU), and warmup during 3% of the training steps. We carry out single-stage fine-tuning for three epochs. During inference, we employ 32-bit full precision to decode up to 150 tokens with a batch size of 1.

6.3.3 Results analysis

Table 5 reports downstream radiology report generation performance on MIMIC-CXR and IU-Xray using a fixed Vicuna-7B language decoder and frozen image encoders. Across both datasets and all evaluation metrics, *RadJEPA* consistently achieves the strongest performance among image-only, predictive, and vision-language pretrained encoders. On MIMIC-CXR, RadJEPA attains the best ROUGE-L (**26.1**), BLEU-4 (**10.1**), R_{GER} (**23.8**), and Macro-F1-14 (**32.6**), outperforming RAD-DINO, I-JEPA, and prior vision-language models. Similar gains are observed on IU-Xray, where RadJEPA improves ROUGE-L by **+1.7**, R_{GER} by **+0.9**, and Macro-F1-14 by **+1.3** over the strongest non-JEPA baseline, indicating generaliza-

tion to an unseen clinical dataset. These improvements are achieved despite RadJEPA operating at a lower input resolution than contrastive baselines such as RAD-DINO.

To ensure fair comparison with prior methods trained exclusively on MIMIC-CXR, we additionally report *control* variants that restrict pretraining data to MIMIC images only. Under this controlled setting, RadJEPA-control consistently matches or outperforms architecture-matched baselines, and the full RadJEPA model further improves performance when pretrained on the larger multi-institutional dataset. This comparison isolates the contribution of the JEPA-style predictive objective from dataset scale alone, demonstrating that performance gains stem from superior image representations rather than increased training data.

7 Significance Analysis

We evaluate the statistical reliability of the observed improvements using single-tailed hypothesis tests, where the null hypothesis assumes no improvement over the baseline. Table 6 summarizes the results across all tasks and datasets, with rows

Metric	V-AP	RSNA	MIM-S	V-Rib	MIM	IU
LO	✓✓					
CM	✗					
PL-T	✓✓					
AE	✓✓					
PF	✓✓					
PE	✗					
AP		✓✓				
AUC		✓✓				
Lung			✓			
L-Zone			✓✓			
Rib			✓✓			
R-L				✓✓	✓✓	
B-4				✓✓	✓✓	
RGER				✓✓	✓✓	
F1				✓✓	✓✓	

Table 6: Single-tailed statistical significance across datasets. V-AP: VinDr-CXR (AP), MIM-S: MIMIC-CXR (Subset), V-Rib: VinDR-RibCXR. ✓✓: statistically significant improvement ($p < 0.05$); ✓: improvement observed but not statistically significant; ✗: no improvement over baseline.

corresponding to evaluation metrics and columns to datasets. Statistically significant improvements are denoted by ✓✓ ($p < 0.05$), improvements that do not reach statistical significance by ✓, and worse performance by ✗, while empty cells indicate non-evaluated metric–dataset pairs. Overall, 16 out of 19 evaluated cases show statistically significant improvements, one case shows a non-significant improvement, and two cases exhibit worse performance than the SoTA baseline, demonstrating that the RadJEPA achieves consistent and statistically reliable gains across diverse evaluation settings.

8 Data and Model Availability

This study uses a combination of public datasets including CheXpert v1.0³, ChestX-ray14⁴, Padchest⁵, VinDR-RibCXR⁶, RSNA-Pneumonia⁷, and IU-Xray⁸. Restricted datasets available via Phys-

³<https://stanfordmlgroup.github.io/competitions/chexpert/>
⁴<https://nihcc.app.box.com/v/ChestXray-NIHCC>
⁵<https://bimcv.cipf.es/bimcv-projects/padchest/>
⁶<https://vindr.ai/datasets/ribcxr>
⁷<https://www.kaggle.com/c/rsna-pneumonia-detection-challenge>
⁸<https://www.kaggle.com/datasets/raddar/chest-xrays-indiana-university>

ioNet include MIMIC-CXR v2.0.0⁹, VinDr-CXR v1.0.0¹⁰, Chest ImaGenome v1.0.0¹¹, BRAX v1.1.0¹², and lung segmentation annotations for MIMIC-CXR v1.0.0¹³. Pretrained weights and source code for all baseline image encoders were obtained from public repositories, including CLIP ViT-L/14¹⁴, CLIP ViT-L/14@336¹⁵, BioViL-T¹⁶, BiomedCLIP¹⁷, MRM¹⁸, DINoV2¹⁹, and Rad-DINO²⁰; all models were used in accordance with their respective licenses.

9 Conclusion

In this work, we introduced RadJEPA, a self-supervised framework for learning radiology image representations without language supervision. By predicting latent representations of masked image regions, RadJEPA departs from both vision–language pre-training and traditional distillation-based architectures, enabling the model to learn directly from unlabeled chest X-ray images. Across disease classification, semantic segmentation, and report generation tasks, RadJEPA exceeds state-of-the-art methods, achieving an aggregate AUPRC improvement of 2–4 points in classification, Dice score gains of 2–5 points in segmentation, and consistent improvements in report generation metrics (e.g., ROUGE-L). These gains are statistically significant under a one-tailed test in 16 out of 19 evaluated settings, demonstrating that strong and general-purpose radiology encoders can be learned without reliance on paired image–text data or traditional distillation-type architectures. Additionally, to support reproducibility and further research, the model checkpoint is released on Hugging Face. Due to the limited scope of this study, we do not explore alternative encoder architecture adaptations (e.g., multi-scale backbones), which we leave for future work.

⁹<https://doi.org/10.13026/C2JT1Q>

¹⁰<https://doi.org/10.13026/3akn-b287>

¹¹<https://doi.org/10.13026/wv01-y230>

¹²<https://doi.org/10.13026/grwk-yh18>

¹³<https://physionet.org/content/lung-segment-mimic-cxr/1.0.0/>

¹⁴<https://huggingface.co/openai/clip-vit-large-patch14>

¹⁵<https://huggingface.co/openai/clip-vit-large-patch14-336>

¹⁶<https://huggingface.co/microsoft/BiomedVLP-BioViL-T>

¹⁷https://huggingface.co/microsoft/BiomedCLIP-PubMedBERT_256-vit_base_patch16_224

¹⁸<https://github.com/RL4M/MRM-pytorch>

¹⁹<https://github.com/facebookresearch/dinov2>

²⁰<https://huggingface.co/microsoft/rad-dino>

References

MD Anouk Stein, Carol Wu, Chris Carr, George Shih, Jamie Dulkowski, kalpathy, Leon Chen, Luciano Prevedello, MD Marc Kohli, Mark McDonald, Peter, Phil Culliton, Safwan Halabi MD, and Tian Xia. 2018. Rsna pneumonia detection challenge. <https://kaggle.com/competitions/rsna-pneumonia-detection-challenge>. Kaggle.

Mahmoud Assran, Quentin Duval, Ishan Misra, Piotr Bojanowski, Pascal Vincent, Michael Rabbat, Yann LeCun, and Nicolas Ballas. 2023a. Self-supervised learning from images with a joint-embedding predictive architecture. In *Proceedings of the IEEE/CVF Conference on Computer Vision and Pattern Recognition*, pages 15619–15629.

Mahmoud Assran and 1 others. 2023b. Self-supervised learning from images with a joint-embedding predictive architecture. In *IEEE Conference on Computer Vision and Pattern Recognition*.

Shruthi Bannur, Maximilian Ilse, Oladimeji Farri, Gaspard Pons, and Jean-Baptiste Schiratti. 2023. Learning to exploit temporal structure for biomedical vision–language pretraining. *arXiv preprint arXiv:2301.12018*.

Hangbo Bao, Li Dong, Songhao Piao, and Furu Wei. 2022. Beit: Bert pre-training of image transformers. In *International Conference on Learning Representations*.

Benedikt Boecking, Naoto Usuyama, Shruthi Bannur, Daniel C Castro, Anton Schwaighofer, Stephanie Hyland, Maria Wetscherek, Tristan Naumann, Aditya Nori, Javier Alvarez-Valle, and 1 others. 2022. Making the most of text semantics to improve biomedical vision–language processing. In *European conference on computer vision*, pages 1–21. Springer.

Aurelia Bustos, Antonio Pertusa, Jose M. Salinas, and María de la Iglesia-Vayá. 2020. Padchest: A large chest x-ray image dataset with multi-label annotated reports. *Medical Image Analysis*, 66:101797.

Erdi Çallı, Ecem Sogancioglu, Bram Van Ginneken, Kicky G van Leeuwen, and Keelin Murphy. 2021. Deep learning for chest x-ray analysis: A survey. *Medical image analysis*, 72:102125.

Mathilde Caron, Hugo Touvron, Ishan Misra, Hervé Jégou, Julien Mairal, Piotr Bojanowski, and Armand Joulin. 2021. Emerging properties in self-supervised vision transformers. In *Proceedings of the IEEE/CVF international conference on computer vision*, pages 9650–9660.

Ting Chen, Simon Kornblith, Mohammad Norouzi, and Geoffrey Hinton. 2020. A simple framework for contrastive learning of visual representations. In *International Conference on Machine Learning*.

Wei-Lin Chiang, Lianmin Zheng, Ying Sheng, Stefano Angelopoulos, Tianle Li, Dacheng Li, Hao Zhang, Banghua Zhu, Michael I. Jordan, Joseph E. Gonzalez, and Ion Stoica. 2023. Vicuna: An open-source chatbot impressing gpt-4 with 90%* chatgpt quality. *arXiv preprint arXiv:2303.10130*.

Mostafa Dehghani, Josip Djolonga, Basil Mustafa, Piotr Padlewski, Jonathan Heek, Justin Gilmer, Andreas Peter Steiner, Mathilde Caron, Robert Geirhos, Ibrahim Alabdulmohsin, and 1 others. 2023. Scaling vision transformers to 22 billion parameters. In *International conference on machine learning*, pages 7480–7512. PMLR.

Karan Desai and Justin Johnson. 2021. Virtex: Learning visual representations from textual annotations. In *Proceedings of the IEEE/CVF conference on computer vision and pattern recognition*, pages 11162–11173.

Xiaoyi Dong, Jianmin Bao, Yinglin Zheng, Ting Zhang, Dongdong Chen, Hao Yang, Ming Zeng, Weiming Zhang, Lu Yuan, Dong Chen, and 1 others. 2023. Maskclip: Masked self-distillation advances contrastive language-image pretraining. In *Proceedings of the IEEE/CVF conference on computer vision and pattern recognition*, pages 10995–11005.

Zijian Dong, Ruilin Li, Yilei Wu, Thuan Tinh Nguyen, Joanna Chong, Fang Ji, Nathanael Tong, Christopher Chen, and Juan Helen Zhou. 2024. Brain-jepa: Brain dynamics foundation model with gradient positioning and spatiotemporal masking. *Advances in Neural Information Processing Systems*, 37:86048–86073.

Kaiming He, Xinlei Chen, Saining Xie, Yanghao Li, Piotr Dollár, and Ross Girshick. 2022. Masked autoencoders are scalable vision learners. In *IEEE Conference on Computer Vision and Pattern Recognition*.

Kaiming He, Haoqi Fan, Yuxin Wu, Saining Xie, and Ross Girshick. 2020. Momentum contrast for unsupervised visual representation learning. In *IEEE Conference on Computer Vision and Pattern Recognition*.

Zhicheng Huang, Xiaojie Jin, Chengze Lu, Qibin Hou, Ming-Ming Cheng, Dongmei Fu, Xiaohui Shen, and Jiashi Feng. 2023. Contrastive masked autoencoders are stronger vision learners. *IEEE Transactions on Pattern Analysis and Machine Intelligence*, 46(4):2506–2517.

Jeremy Irvin, Pranav Rajpurkar, Michael Ko, Yifan Yu, Mihaela Ciurea-Ilinca, Chris Chute, Henrik Marklund, Babak Haghgoo, Robyn Ball, Katie Shpanskaya, and 1 others. 2019. Chexpert: A large chest radiograph dataset with uncertainty labels and expert comparison. In *Proceedings of the AAAI Conference on Artificial Intelligence*, volume 33, pages 590–597.

Fabian Isensee, Jens Petersen, Andre Klein, David Zimerer, Paul F. Jaeger, Simon Kohl, Jakob Wassermann,

Gregor Koehler, Tobias Norajitra, Sebastian Wirkert, and Klaus H. Maier-Hein. 2018. nnu-net: Self-adapting framework for u-net-based medical image segmentation. *arXiv preprint arXiv:1809.10486*.

Alistair EW Johnson, Tom J Pollard, Seth J Berkowitz, Nathaniel R Greenbaum, Matthew P Lungren, Chih-ying Deng, Roger G Mark, and Steven Horng. 2019. Mimic-cxr, a de-identified publicly available database of chest radiographs with free-text reports. *Scientific data*, 6(1):317.

Charles Jones, Daniel C Castro, Fabio De Sousa Ribeiro, Ozan Oktay, Melissa McCradden, and Ben Glocker. 2024. A causal perspective on dataset bias in machine learning for medical imaging. *Nature Machine Intelligence*, 6(2):138–146.

Yann LeCun. 2022. A path towards autonomous machine intelligence. *arXiv preprint arXiv:2207.09215*.

Yanghao Li, Hanzi Mao, Ross Girshick, and Kaiming He. 2022. Exploring plain vision transformer backbones for object detection. In *European Conference on Computer Vision (ECCV)*.

Paul Pu Liang and 1 others. 2022. Mind the gap: Understanding the modality gap in vision–language models. In *Advances in Neural Information Processing Systems*.

Haotian Liu, Chunyuan Li, Qingyang Wu, and Yong Jae Lee. 2023a. Improved baselines with visual instruction tuning. *arXiv preprint arXiv:2306.06202*.

Haotian Liu, Chunyuan Li, Qingyang Wu, and Yong Jae Lee. 2023b. Visual instruction tuning. *arXiv preprint arXiv:2304.08485*.

Ha Q Nguyen, Khanh Lam, Linh T Le, Hieu H Pham, Dat Q Tran, Dung B Nguyen, Dung D Le, Chi M Pham, Hang TT Tong, Diep H Dinh, and 1 others. 2022. Vindr-cxr: An open dataset of chest x-rays with radiologist’s annotations. *Scientific Data*, 9(1):429.

Hoang C Nguyen, Tung T Le, Hieu H Pham, and Ha Q Nguyen. 2021. Vindr-ribcxr: A benchmark dataset for automatic segmentation and labeling of individual ribs on chest x-rays. *arXiv preprint arXiv:2107.01327*.

Aaron van den Oord, Yazhe Li, and Oriol Vinyals. 2018. Representation learning with contrastive predictive coding. *arXiv preprint arXiv:1807.03748*.

Maxime Oquab, Timothée Darcet, Théo Moutakanni, Huy Vo, Marc Szafraniec, Vasil Khalidov, Pierre Fernandez, Daniel Haziza, Francisco Massa, Alaaeldin El-Nouby, and 1 others. 2023. Dinov2: Learning robust visual features without supervision. *arXiv preprint arXiv:2304.07193*.

Fernando Pérez-García, Harshita Sharma, Sam Bond-Taylor, Kenza Bouzid, Valentina Salvatelli, Maximilian Ilse, Shruthi Bannur, Daniel C Castro, Anton Schwaighofer, Matthew P Lungren, and 1 others. 2024. Rad-dino: Exploring scalable medical image encoders beyond text supervision. *arXiv preprint arXiv:2401.10815*.

Fernando Perez-Garcia, Harshita Sharma, Sam Bond-Taylor, Kenza Bouzid, Valentina Salvatelli, Maximilian Ilse, Shruthi Bannur, Daniel C Castro, Anton Schwaighofer, Matthew P Lungren, and 1 others. 2025. Exploring scalable medical image encoders beyond text supervision. *Nature Machine Intelligence*, 7(1):119–130.

Alec Radford, Jong Wook Kim, Chris Hallacy, Aditya Ramesh, Gabriel Goh, Sandhini Agarwal, Girish Sastry, Amanda Askell, Pamela Mishkin, Jack Clark, and 1 others. 2021. Learning transferable visual models from natural language supervision. In *International conference on machine learning*, pages 8748–8763. PMLR.

Eduardo P. Reis, Maurício J. Cardoso, Filipe Cordeiro, João F. Teixeira, Victor Alves, Hugo Silva, and 1 others. 2022. Brax: A large-scale radiology dataset for benchmarking chest x-ray algorithms. *Scientific Data*, 9(1):1–10.

Mingxing Tan and Quoc V. Le. 2019. Efficientnet: Rethinking model scaling for convolutional neural networks. *International Conference on Machine Learning (ICML)*.

Yucheng Tang and 1 others. 2022. Self-supervised learning of medical image representations via relation-driven masking. *IEEE Transactions on Medical Imaging*.

Ethan Tiu, Yifan Peng, Michael Zhou, Pranav Rajpurkar, Matthew P. Lungren, and Andrew Y. Ng. 2022. Expert-level zero-shot learning for chest x-ray interpretation. *arXiv preprint arXiv:2206.12068*.

Xiaosong Wang, Yifan Peng, Le Lu, Zhiyong Lu, Mohammad Bagheri, and Ronald M. Summers. 2017. Chestx-ray8: Hospital-scale chest x-ray database and benchmarks on weakly-supervised classification and localization of common thorax diseases. *Proceedings of the IEEE Conference on Computer Vision and Pattern Recognition (CVPR)*, pages 3462–3471.

Joy T Wu, Nkechinyere N Agu, Ismini Lourentzou, Arjun Sharma, Joseph A Paguio, Jasper S Yao, Edward C Dee, William Mitchell, Satyananda Kashyap, Andrea Giovannini, and 1 others. 2021. Chest imangenome dataset for clinical reasoning. *arXiv preprint arXiv:2108.00316*.

Tete Xiao, Yingcheng Liu, Bolei Zhou, Yuning Jiang, and Jian Sun. 2018. Unified perceptual parsing for scene understanding. In *European Conference on Computer Vision (ECCV)*.

Xiaohua Zhai and 1 others. 2022. Lit: Zero-shot transfer with locked-image text tuning. In *IEEE Conference on Computer Vision and Pattern Recognition*.

Yuhao Zhang, Yu Wang, Yuhui Zhang, Zhe Li, and Yifan Xu. 2023. Large-scale domain-specific vision-language pretraining for biomedical applications. *arXiv preprint arXiv:2303.00915*.

Lianmin Zheng, Wei-Lin Chiang, Ying Sheng, Siyuan Zhuang, Zhanghao Wu, Yonghao Zhuang, Zi Lin, Zhuohan Li, Dacheng Li, Eric Xing, and 1 others. 2023. Judging llm-as-a-judge with mt-bench and chatbot arena. *Advances in neural information processing systems*, 36:46595–46623.

Hong-Yu Zhou, Chenyu Lian, Liansheng Wang, and Yizhou Yu. 2023. Advancing radiograph representation learning with masked record modeling. *arXiv preprint arXiv:2301.13155*.

Zongwei Zhou and 1 others. 2019. Models genesis: Generic autodidactic models for 3d medical image analysis. In *International Conference on Medical Image Computing and Computer-Assisted Intervention*.